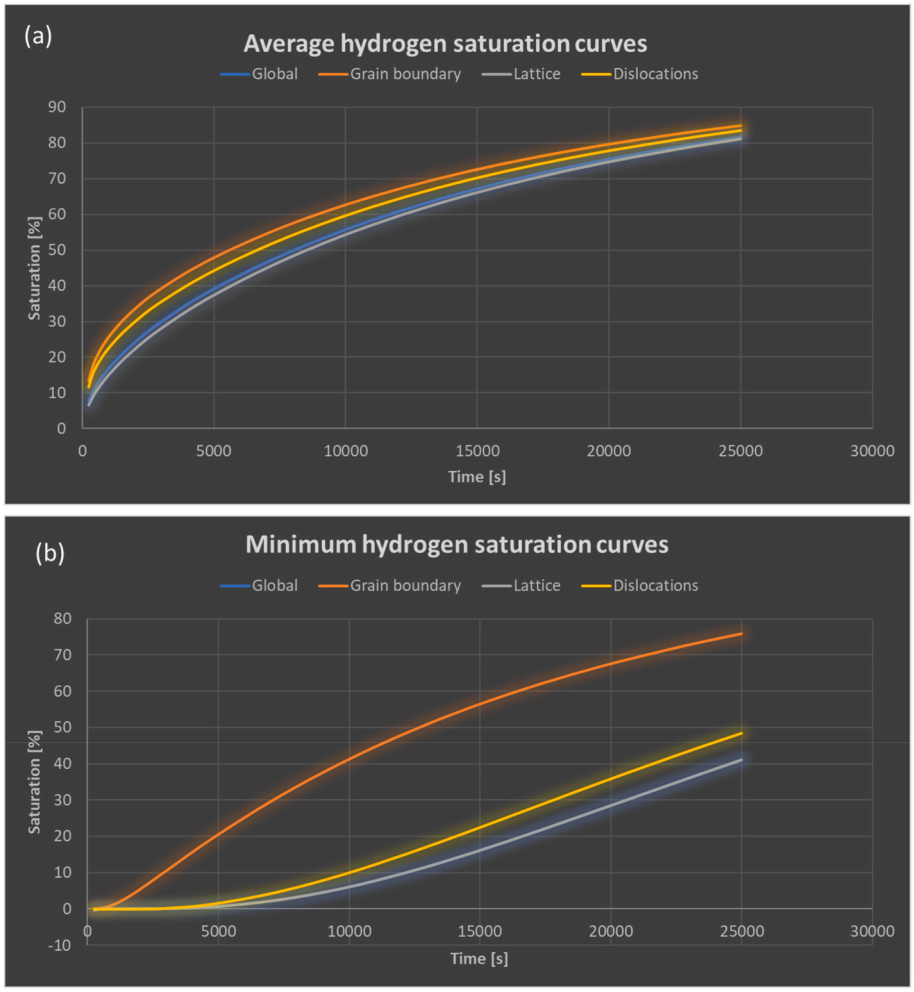

Fig. 15. (a) Saturation curves, (b) Minimum saturation curves of the final model.

than the limit that makes the precipitate saturated, then the mesh around the precipitate is refined to simulate the saturation effect.

It is possible that not all precipitates are saturated, for this reason and to lighten the computation load of the model, the saturated precipitates will be meshed. Precipitates are of four different categories, so four limiting concentrations are used for calculations in macros. The first simulation (no precipitates) contains only the grain boundary and the dislocations as traps.

Table 9 summarized the precipitates calculation for a temperature equals to 300 K.

Knowing number of the saturated precipitates the mesh is updated to considering the precipitate effect.

Fig. 9 (c) shows the nodal solution for the model after the implementation of the precipitates. Also in this case the main effects of the precipitates occur in the grain boundary (higher saturation level), in particular the elements of the precipitates have lower saturations than those of the grain boundary.

The next step concerns the implementation of a microstructure formed by several grains and the subsequent simulation.

The microstructure is formed by 17 truncated octagon grains surrounded by grain boundaries phases. The dimension of geometry is reported in Table 10.

The geometry analysed in the model is composed by 184 grains. The volume is formed by a cube in which 9 grains are placed on each side. Fig. 10 (a) show the geometry implemented on the model. Table 11 summarize the geometrical characteristic of the volume.

This geometry was chosen to be able to analyze the phenomenon of diffusion on an adequate scale in order to obtain physically acceptable results from the model.

To manipulate the model results, the mesh must be adequate. To make this possible it is necessary that the elements of the mesh are on average of the same volume, moreover it is necessary to mesh first the grain boundary and then the grain. Using this meshing method, it's possible to get that the ID number of the first elements and nodes belongs to the grain boundary, the second group of elements and nodes belongs to the grain. Fig. 10 (b) shows the mesh implementation. Table 12 shows the summarized results for the mesh calculation.

The first Macro that is generated is called "EXPORT NUMBER OF NODES AND ELEMENTS". This macro is written in APDL, and it's able to export all the mesh statistics from the Ansys model to texts files. After the export it's possible to manipulate the results to generate the precipitates and the dislocation elements.

An interface has been created to be able to enter the model inputs, that are: working temperature and volume of the geometry. In the interface it is also necessary to select the workbook to guarantee the correct dialogue between macros, Ansys Workbench, and python scripts. The code will automatically calculate the hydrogen diffusion coefficient for all the material by using the working temperature, these results for300 K are reported in Table 13.

Script called "DISLOCATION" is implemented by using Python. This code is able to read all the results exported by [Appendix 1] and the input data from the Interface to calculate the number of elements that will simulate the dislocation effects.

Table 14 summarized the results for the dislocation calculation.

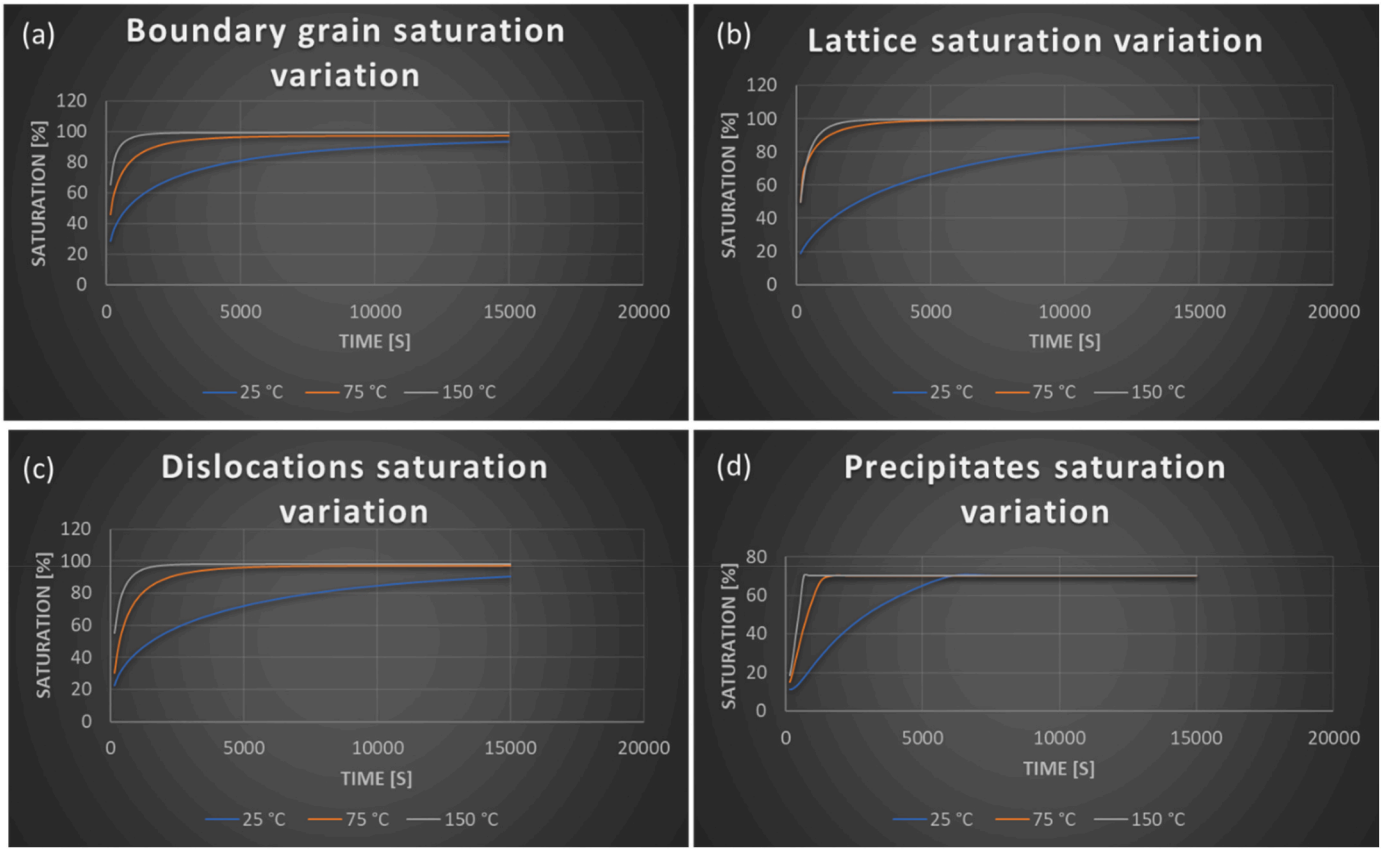

Fig. 16. Level of saturation in function of the temperature. Grain boundary saturation variation (a), lattice saturation variation (b), dislocation saturation variation (c), precipitate saturation variation (d).

This script generates the input for the second Python scrips. In this file there are the total elements number for the geometry, the element number for the boundary grain, the total node number for the geometry, the node number for the boundary grain and the element number for the dislocation. it is used to decrease the level of mathematical calculation that each script has, in fact the export procedure of the number of elements and nodes from Ansys Workbench and the reading of these files are the slowest processes of the whole model.

The second script is called "dislocation generation". This code can read the output of the "DISLOCATION" script and to generate a macro in APDL who can be read by Ansys Workbench to implement the dislocation. In this code the number of elements of the dislocation is read and it's converted to number of nodes. Knowing the number of the nodes of the dislocation it's possible to generate the macro who creates the dislocations in the grain. The ID number of the nodes in the grain are chose randomly. The output generated by this script is a macro called "ND_disl", whit this macro it's possible to create named sections who will represent the node of dislocation and the element of dislocation, this macro changes the material properties of the dislocation elements. [Appendix 2].

After the mesh updating it's necessary to launch the first transient thermal simulation. The behaviour of the microstructure is simulated as a consequence of a hydrogen saturated atmosphere adjacent to one side of the geometry. Concentration equals to 100 % is used. Fig. 10 (c) and Table 15 shows the set-up of the thermal analysis.

The nodal results must be exported as a text file for the consistency of the model, it's necessary to create a text file called "SATURATION_NODE_0. txt" [Appendix 3].

Fig. 11 shows the elements solution for this simulation.

The second and last section of the model begins with the analysis of the precipitates. Python is used to implement scripts that are used to generate macros that can simulate the effect of precipitates. The first step is the importation of the results of the previous section, i.e., operating temperature, number, and ID of the elements of the dislocations and the nodal results.

After that it's possible to manipulate the input data. The 70 % of the total precipitates are in the grain boundary, the remainder in the grain. Knowing the maximum concentration of hydrogen that each precipitate can contain, it is possible to know the number of saturated precipitates.

The next step includes the generation of a macro that creates components in Ansys Workbench that contain the nodes and elements of each type of precipitate. This macro is called "PRECIPITATES" [Appendix 4]. For this macro it's used a Fortran format descriptors "8i10". Table 16 summarized the results for the precipitates calculation. In this case not all the precipitates are saturated, only 12 % of the precipitates are saturated.

The last step is the thermal simulation. The same settings of the last simulation will be used. The nodal results must be exported as a text file for successive analysis, it's necessary to create a text file called "SATURATION_NODE_1. txt" [Appendix 5].

Fig. 12 shows the nodal solutions of the grain boundary saturation during the simulation, the diffusion process is uniform over time.

Fig. 13 shows the nodal solutions of the grain saturation during the simulation, also in this case the diffusion path is strongly influenced by the presence of dislocations which modify the hydrogen saturation in the grain.

Fig. 14 shows the nodal solutions for the total geometry during the simulation.

The simulated geometry has a volume of 28 668 [um^3], All saturation curves simulate the average evolution of hydrogen saturation for the volume of the geometry. A saturation equal to 100 % indicates that the entire volume has reached the maximum capacity of hydrogen

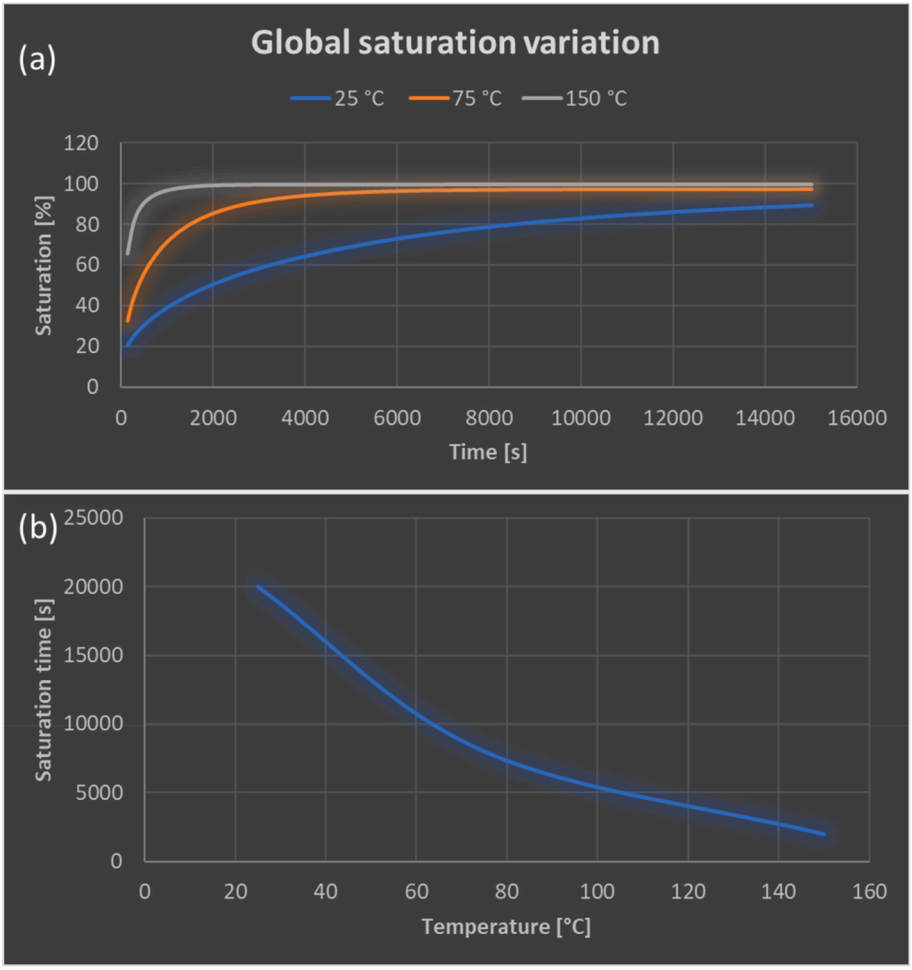

Fig. 17. (a)Level of global saturation and (b) Saturation time, in function of the temperature.

Table 17
Saturation time in function of the temperature.

Temperature [°C]	Saturation time [s]
25	20 000
75	8000
150	2000

atoms. Fig. 15(a) shows the trend of the average saturations for grain boundary, grain and dislocations for a time interval ranging from 0 s to 25 000 s. The average saturation of the grain boundary at the end of the simulation reaches a value of 84.9 %. This value is based on the grain boundary volume which is 6967 [um^3]. Again, the mean saturation curve of the grain boundary tends fastest to the horizontal asymptote representing the full saturation value (100 %). The second fastest saturation curve is that of the dislocations. At the end of the simulation (25 000 s) the dislocations reach an average saturation level of 83.5 % (based on a volume of 2170 [um^3]). The saturation curve of the lattice is the least rapid, at the end of the simulation (25 000 s) a maximum saturation level of 81.1 % is reached on a volume of 21 701 [um^3]. The global saturation curve is strongly dependent on that of the grain due to its volume, in fact the volume of the grain is equal to 75 % of the total volume. At the end of the simulation the global saturation is 81.8 %.

Subsequently, the minimum saturation change in the microstructure is analysed. With this analysis it is possible to obtain the saturation trend of the microstructure portions which are last reached by the hydrogen diffusion path. The minimum saturation curves are shown in Fig. 15 (b). The grain boundary is the portion of the volume that first diffuses the hydrogen, by analyzing the minimum saturation curves it is possible to notice that the minimum saturation value in the grain boundary increases rapidly with time, in fact after 5000 s the minimum saturation value of all the volume of the grain boundary is 20 %. After 5000 s of simulation the minimum saturation value in the grain and in the dislocations does not exceed 5 %. To obtain a minimum saturation value of 20 %, it takes 14 000 s for the dislocations and 17 000 s for the grain, respectively. The minimum saturation trend of the entire microstructure is superimposed on that of the lattice, this effect occurs because the lattice is the largest volumetric portion within the microstructure. The final performed simulations concern the analysis of the effectiveness of the model for simulations carried out at various working temperatures. Fig. 16 shows the variation of the main outputs as the temperature varies. All results refer to a total microstructure of 3560 [um^3].

Fig. 16(a) shows how the saturation of the grain boundary in function of the time and temperatures. Since the diffusive coefficient of the grain boundary increases with the increase of the absolute temperature, the saturation trend is consistent with this physical concept. In particular, the average saturation of the grain boundary has a percentage increase of 8.7 % for a temperature of 75 °C and an average percentage increase of 11.4 % for a temperature of 150 °C (respect to 25 °C). These temperatures have been chosen based on the thermal range to which an austenitic stainless steel is subjected.

Fig. 16(b) shows the change in grain saturation for three temperatures. Also in this case the diffusive coefficient of the grain increases with the increase of the absolute temperature, the saturation trend is consistent with this physical concept. In particular, the average

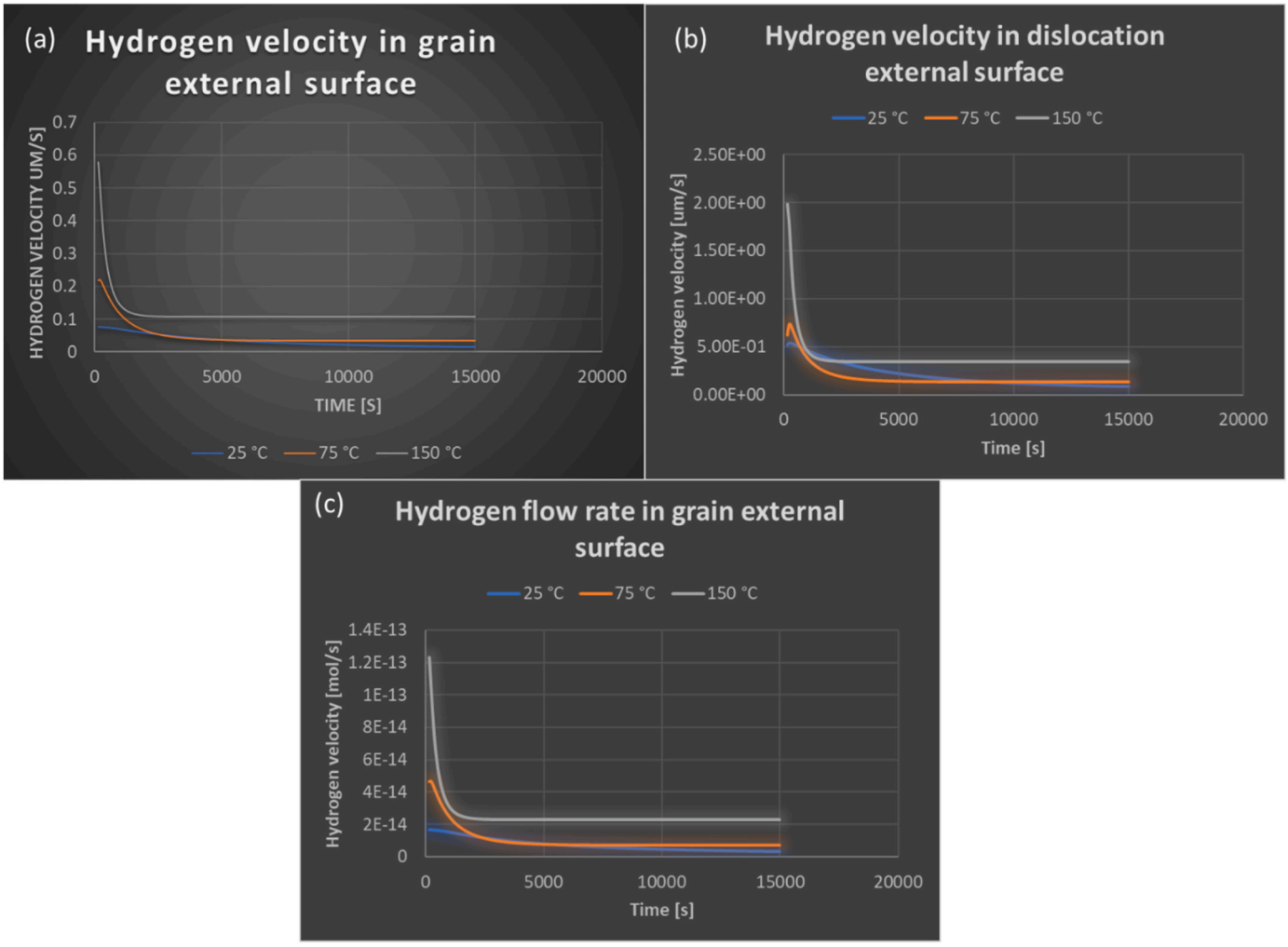

Fig. 18. (a) Hydrogen velocity in grain boundary-grain interface, (b) Hydrogen velocity in dislocation-grain interface, (c) Hydrogen flow rate in grain boundary-grain interface.

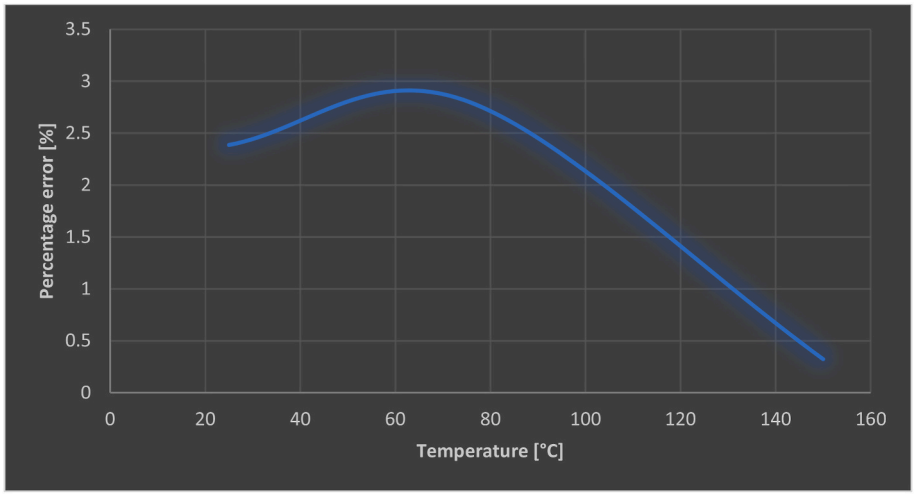

Fig. 19. error in function after the precipitates implementation in function of the temperature.

saturation of the grain has a percentage increase of 4.1 % for a temperature of 75 °C and an average percentage increase of 6.4 % for a temperature of 150 °C.

The results show that grain saturation is less affected by the increase in temperature than boundary grain.

Fig. 16(c) shows how the effect of dislocations varies with the temperature. The number of dislocations depends on the temperature, as the temperature increases there is a decrease in the number of dislocations.

However, the decrease of the elements of the dislocations is accompanied by an increase in the diffusion coefficient of the dislocations themselves. Thus, even though the number of dislocations is decreasing, their saturation level increases with temperature.

Fig. 16(d) shows the level of saturation of the precipitates as the working temperature varies. In this thesis the number of precipitates is considered fixed as the temperature varies, however as the temperature increases there is an increase in the diffusion properties of the entire microstructure, this increase favours the saturation of the precipitates which as the temperature increases tend to be all saturated with hydrogen.

Fig. 17 shows the trend of the global saturation variation. Table 17 shows the times necessary for the maximum saturation of the simulated geometry as a function of time. Using these values, it is possible to trace a trend of the total saturation times of the simulated geometry as a function of time and temperature.

Fig. 18 shows the average velocity of hydrogen particles passing through the grain boundary interface in function of the time. The calculation is made with the following assumptions:

$$c_{p_H} = 14304 \left[\frac{j}{kgK}\right]$$

$$\rho_H = 0.0899 \left[\frac{kg}{m^3}\right]$$

$$v_{m_H} = 11.42 * 10^{-3} \left[\frac{m^3}{mol}\right]$$

$$A_{Lat_{GB}} = 2425.5 \left[um^2\right]$$

where c_{p_H} is the hydrogen specific heat, ρ_H is the hydrogen density, v_{m_H} is the hydrogen molar volume and $A_{lat_{GB}}$ is the area of the interface between grain and boundary grain. Fig. 18 shows the results for three temperatures (25 °C, 75 °C and 150 °C). The velocity profile of the flow of hydrogen atoms in surface A passing from the grain boundary to the grain decreases with increasing time. This phenomenon is due to the increase in saturation of the microstructure with the time which requires less flow of hydrogen with increasing time (to saturate the model). The mean speed of the flow increases with the increase of the temperature and with it also the modulus of the asymptotic value to which it tends.

Fig. 18 (b) shows the average velocity of hydrogen particles passing through the dislocation-grain interface. In this case the value of the mean velocity is greater than the value of the boundary grain-grain interface. Fig. 18 (c) shows the hydrogen flow rate in grain boundary-grain interface in function of the time and temperature. The hydrogen flow rate has the same trend of the hydrogen velocities. Also, in this case the explanation for this phenomenon is the global increase in saturation over time. this increase leads to a reduction in the speed and flow rate of hydrogen in the microstructure. The flow rate of hydrogen tends to decrease until it stops for the time of complete saturation.

An error analysis was performed to verify that the generated model is mathematically correct. To do this, it is necessary to compare the values of the nodal temperatures around the precipitates before and after the implementation of the latter. An error of less than 7 % is considered acceptable for this type of analysis.

The error analysis was carried out for three temperatures in order to have a trend of the robustness of the model as a function of the temperature. The percentage errors generated by the model as the temperature varies are shown in Fig. 19. From the error analysis it emerges that the model has an error of less than 3 % in all the simulated temperatures. This result demonstrates the reliability of the model as the temperature varies.

The simulations movies describing the diffusion behaviour are shown in Supplementary material.

4. Conclusions

The model simulates the diffusion of hydrogen in an austenitic stainless-steel microstructure. It is possible to modify the material properties to simulate the diffusion of hydrogen for various types of microstructures. Three different grain sizes have been implemented in the model, by modifying the geometry it is possible to simulate the diffusion of hydrogen for grains of different sizes and shapes in such a way as to adapt the model to the desired microstructure. It is possible to implement microstructures with asymmetric grains and of various crystalline structures.

The future developments that can be included in this model mainly concern three points: implement the phenomenon of hydrogen diffusion for a material subjected to a non-zero stress and to couple the dependence on temperature to that on mechanical stress. Optimize the model in order to increase the calculation speed. This could extend the use of the model to geometries of orders of magnitude greater than a millimetre. Adapt the macros in such a way as to be able to obtain valid trap calculations for each type of microstructure.

CRediT authorship contribution statement

P. Cavaliere: Conceptualization, Data curation, Methodology, Project administration, Supervision. **B. Sadeghi:** Data curation, Investigation. **A. Perrone:** Formal analysis, Investigation. **D. Marsano:** Formal analysis, Investigation, Software. **A. Marzanese:** Formal analysis, Investigation, Software.

Declaration of competing interest

The authors declare that they have no known competing financial interests or personal relationships that could have appeared to influence the work reported in this paper.

Data availability

Data will be made available on request.

Acknowledgments

The Authors would like to thank the Department of Innovation Engineering for the Grant provided to Pasquale Cavaliere "Reattori innovativi per l'utilizzo di idrogeno (REIDRO)" in Ricerca di Base 2023

Appendix A. Supplementary data

Supplementary data to this article can be found online at https://doi.org/10.1016/j.ijpvp.2023.105120.

[Appendix 1] EXPORT NUMBER OF NODES AND ELEMENTS

```
NSLE,S.
*VGET, Totali_nd,NODE,ALL,NSEL,2.
*CREATE, ansuitmp.
*CFOPEN,'Totali_nodi','txt',' '.
*VWRITE, Totali_nd (1,1), , , ,
(F100.0).
*CFCLOS.
*END.
/INPUT, ansuitmp.
ALLSEL,all.
CMSEL,S,NS_el_Grani.
*VGET, Totali_el,ELEM,ALL,ESEL,2.
*CFOPEN,'Totali_elem','txt',' '.
*VWRITE, Totali_el (1,1), , , ,
(F100.0).
```

```
CMSEL,S,NS_nd_Grani.
*VGET, NS_nd_Grani1,NODE,ALL,NLIST,2.
*CFOPEN,'NS_nd_Grani','txt',' '.
*VWRITE, NS_nd_Grani1 (1,1), , , ,
(F100.0).
*VGET, NS_el_Grani1,ELEM,ALL,ELIST,2.
*CFOPEN,'NS_el_Grani','txt',' '.
*VWRITE, NS_el_Grani1 (1,1), , , ,
(F100.0).
CMSEL,S,NS_nd_Skin.
*VGET, NS_nd_skin1,NODE,ALL,NLIST,2.
*CFOPEN,'NS_nd_Skin','txt',' '.
*VWRITE, NS_nd_Skin1 (1,1), , , ,
(F100.0).
CMSEL,S,NS_el_Skin.
*VGET, NS_el_Skin1,ELEM,ALL,ELIST,2.
*CFOPEN,'NS_el_Skin','txt',' '.
*VWRITE, NS_el_Skin1 (1,1), , , ,
(F100.0).
```

[Appendix 2] ND_disl

```
/sys,python DISLOCATION. py.
/sys,python dislocation_generation.py.
FLST,5,330,2,ORDE,330.
FITEM,5,20 148.
NSEL,S,P51X
CM,DISL_N,NODE.
CMSEL,S,DISL_N.
ESLN,S.
CM,DISL_E,ELEM.
MPCHG,3,ALL,
ALLSEL,ALL.
```

[Appendix 3] SATURATION_NODE_0

```
Node ID Saturation []
1 67.
2 67.1.
3 59.
```

[Appendix 4] PRECIPITATES

```
CMBLOCK, PRECG1,NODE,45.
(8i10)
7622 10 347 7094 336 10 528 11 651 12 699 1914.
CMBLOCK, PRECG2A,NODE,115.
(8i10)
11 815 13 305 2225 9289 1977 12 883 4317 9005.
CMBLOCK, PRECG2B,NODE,58.
(8i10)
1005 1293 27 286 19 470 25 427 22 395 15 408 22 044.
CMBLOCK, PRECG3,NODE,15.
(8i10)
13 399 18 198 23 148 22 036 27 606 26 820 25 093 16 520.
CMSEL,S,PRECG1.
CM,PRECG1_E,ELEM.
CMSEL,S,PRECG1_E.
MPCHG,2,ALL,
ALLSEL,ALL.
CMSEL,S,PRECG2A.
CM,PRECG2A_E,ELEM.
CMSEL,S,PRECG2A_E.
CMSEL,S,PRECG2B.
CM,PRECG2B_E,ELEM.
CMSEL,S,PRECG2B_E.
CMSEL,S,PRECG3.
CM,PRECG3_E,ELEM.
CMSEL,S,PRECG3_E.
[Appendix 5] SATURATION_NODE_0
```

References

[1] H.K. Birnbaum, P. Sofronis, Hydrogen-enhanced localized plasticity—a mechanism for hydrogen-related fracture, Mater. Sci. Eng., A 176 (1) (1994) 191–202.
[2] I.M. Robertson, P. Sofronis, A. Nagao, M.L. Martin, S. Wang, D.W. Gross, K. E. Nygren, Hydrogen embrittlement understood, Metall. Mater. Trans. 46 (6) (2015) 2323–2341.
[3] S. Bechtle, M. Kumar, B.P. Somerday, M.E. Launey, R.O. Ritchie, Grain-boundary engineering markedly reduces susceptibility to intergranular hydrogen embrittlement in metallic materials, Acta Mater. 57 (14) (2009) 4148–4157.
[4] M. Koyama, C.C. Tasan, E. Akiyama, K. Tsuzaki, D. Raabe, Hydrogen-assisted decohesion and localized plasticity in dual-phase steel, Acta Mater. 70 (2014) 174–187.
[5] M. Nagumo, M. Nakamura, K. Takai, Hydrogen thermal desorption relevant to delayed-fracture susceptibility of high-strength steels, Metall. Mater. Trans. 32 (2001) 339–347.
[6] I. Moro, L. Briottet, P. Lemoine, E. Andrieu, C. Blanc, G. Odemer, Hydrogen embrittlement susceptibility of a high strength steel X80, Mater. Sci. Eng., A 527 (27–28) (2010) 7252–7260.
[7] WHAT IS HYDROGEN EMBRITTLEMENT?, CAUSES, Effects and Prevention. https://www.twi-global.com/technical-knowledge/faqs/what-is-hydrogen-embrittlement.
[8] O. Barrera, D. Bombac, Y. Chen, T.D. Daff, E. Galindo-Nava, P. Gong, D. Haley, R. Horton, I. Katzarov, J.R. Kermode, C. Liverani, M. Stopher, F. Sweeney, Understanding and mitigating hydrogen embrittlement of steels: a review of experimental, modelling and design progress from atomistic to continuum, J. Mater. Sci. 53 (9) (2018) 6251–6290.
[9] M.S. Daw, M.I. Baskes, Semiempirical, quantum mechanical calculation of hydrogen embrittlement in metals, Phys. Rev. Lett. 50 (17) (1983) 1285.
[10] R. Oriani, Hydrogen embrittlement of steels, Annu. Rev. Mater. Sci. 8 (1) (1978) 327–357.
[11] N.-E. Laadel, M. El Mansori, N. Kang, S. Marlin, Y. Boussant-Roux, Permeation barriers for hydrogen embrittlement prevention in metals – a review on mechanisms, materials suitability and efficiency, Int. J. Hydrogen Energy 47 (76) (2022) 32707–32731.
[12] Y. Liu, Y. Chen, C. Yang, J. Lian, Y. Feng, X. Han, The effect of charging conditions on hydrogen embrittlement behavior of ultra-high-strength steel 22MnB5, Mater. Char. 194 (2022) 112377.
[13] L.S. Morrissey, S. Nakhla, Molecular dynamics simulations of the hydrogen embrittlement base case: atomic hydrogen in a defect free single crystal, Mol. Simulat. 48 (13) (2022) 1214–1222.
[14] H.K.D.H. Bhadeshia, Prevention of hydrogen embrittlement in steels, ISIJ Int. 56 (1) (2016) 24–36.
[15] O. Zvirko, E. Kryzhanivskyi, H. Nykyforchyn, H. Krechkovska, Methods for the evaluation of corrosion-hydrogen degradation of steels of oil-and-gas pipelines, Mater. Sci. 56 (2021) 585–592.
[16] H. Nykyforchyn, O. Tsyrulnyk, O. Zvirko, H. Krechkovska, Non-destructive evaluation of brittle fracture resistance of operated gas pipeline steel using electrochemical fracture surface analysis, Eng. Fail. Anal. 104 (2019) 617–625.
[17] Z. Zheng, M. Yi, S. Wang, Abnormal trapping of hydrogen in the elastic stress field of dislocations in body-centered cubic iron, Int. J. Hydrogen Energy 47 (92) (2022) 39255–39264.
[18] S. Leitner, W. Ecker, F.-D. Fischer, J. Svoboda, Thermodynamic trapping and diffusion model for multiple species in systems with multiple sorts of traps, Acta Mater. 233 (2022) 117940.
[19] C. Williams, E. Galindo-Nava, Accelerating off-lattice kinetic Monte Carlo simulations to predict hydrogen vacancy-cluster interactions in α-Fe, Acta Mater. 242 (2023) 118452.
[20] R. Fernández-Sousa, C. Betegón, E. Martínez-Paneda, Cohesive zone modelling of hydrogen assisted fatigue crack growth: the role of trapping, Int. J. Fatig. 162 (2022) 106935.
[21] P. Cavaliere, A. Perrone, D. Marsano, A. Marzanese, B. Sadeghi, Modelling of the hydrogen embrittlement in austenitic stainless steels, Materialia 30 (2023) 101855.
[22] A. McNabb, P. Foster, A New Analysis of the Diffusion of Hydrogen in Iron and Ferritic Steels, Institute of Metals Division, AIME, 1963.
[23] N. Yazdipour, A. Haq, K. Muzaka, E. Pereloma, 2D modelling of the effect of grain size on hydrogen diffusion in X70 steel, Comput. Mater. Sci. 56 (2012) 49–57.
[24] B. Tekkaya, M. Dölz, S. Münstermann, Modeling of local hydrogen concentration on microscopic scale to characterize the influence of stress states and non-metallic inclusions in pipeline steels, Int. J. Hydrogen Energy 50 (2024) 1274–1287.
[25] B.M. Şeşen, M. Mansoor, C. Örnek, Elucidating the dynamics of hydrogen embrittlement in duplex stainless steel, Corrosion Sci. 225 (2023) 111549.
[26] P. Tao, J. Gong, Y. Wang, W. Cen, J. Zhao, Modeling of hydrogen diffusion in duplex stainless steel based on microstructure using finite element method, Int. J. Pres. Ves. Pip. 180 (2020) 104031.
[27] F. Yang, J. Zhang, Y. Zhang, Modeling corrosion product film formation and hydrogen diffusion at the crack tip of austenitic stainless steel, Materials 16 (17) (2023) 5799.

[28] A.H. Krom, A. Bakker, Hydrogen trapping models in steel, Metall. Mater. Trans. B 31 (2000) 1475–1482.
[29] L. Sanchez, H. Cong, AC interference on hydrogen absorption in low carbon steel under cathodic protection, Int. J. Hydrogen Energy 48 (3) (2023) 1202–1217.
[30] A. Díaz, A. Zafra, E. Martínez-Pañeda, J. Alegre, J. Belzunce, I.I. Cuesta, Simulation of hydrogen permeation through pure iron for trapping and surface phenomena characterisation, Theor. Appl. Fract. Mech. 110 (2020) 102818.
[31] V.I. Mironov, I.G. Emel'yanov, O.A. Lukashuk, Criteria of Material Failure in Relation to Hydrogen Saturation, Solid State Phenomena, Trans Tech Publ, 2021, pp. 484–489.
[32] S. Samanta, P. Kumari, K. Mondal, M. Dutta, S.B. Singh, An alternative and comprehensive approach to estimate trapped hydrogen in steels using electrochemical permeation tests, Int. J. Hydrogen Energy 45 (51) (2020) 26666–26687.
[33] O. Barrera, E. Tarleton, H.W. Tang, A.C.F. Cocks, Modelling the coupling between hydrogen diffusion and the mechanical behaviour of metals, Comput. Mater. Sci. 122 (2016) 219–228.
[34] A. Oudriss, J. Creus, J. Bouhattate, E. Conforto, C. Berziou, C. Savall, X. Feaugas, Grain size and grain-boundary effects on diffusion and trapping of hydrogen in pure nickel, Acta Mater. 60 (19) (2012) 6814–6828.
[35] C. Marte, R. Kirchheim, Hydrogen diffusion in nanocrystalline nickel indicating a structural change within the grain boundaries after annealing, Scripta Mater. 37 (8) (1997).
[36] Y.-L. Liu, Y. Zhang, H.-B. Zhou, G.-H. Lu, F. Liu, G.-N. Luo, Vacancy trapping mechanism for hydrogen bubble formation in metal, Phys. Rev. B 79 (17) (2009) 172103.
[37] T. Hickel, R. Nazarov, E.J. McEniry, G. Leyson, B. Grabowski, J. Neugebauer, Ab initio based understanding of the segregation and diffusion mechanisms of hydrogen in steels, JOM 66 (8) (2014) 1399–1405.
[38] J. Hirth, B. Carnahan, Hydrogen adsorption at dislocations and cracks in Fe, Acta Metall. 26 (12) (1978) 1795–1803.
[39] A. Oudriss, J. Creus, J. Bouhattate, C. Savall, B. Peraudeau, X. Feaugas, The diffusion and trapping of hydrogen along the grain boundaries in polycrystalline nickel, Scripta Mater. 66 (1) (2012) 37–40.
[40] M. Nagumo, Fundamentals of Hydrogen Embrittlement, Springer, 2016.
[41] A.A. Guzmán, J. Jeon, A. Hartmaier, R. Janisch, Hydrogen embrittlement at cleavage planes and grain boundaries in bcc iron—revisiting the first-principles cohesive zone model, Materials 13 (24) (2020) 5785.
[42] S. Ueki, R. Oura, Y. Mine, K. Takashima, Micro-mechanical characterisation of hydrogen embrittlement in nano-twinned metastable austenitic stainless steel, Int. J. Hydrogen Energy 45 (51) (2020) 27950–27957.
[43] B. Zhang, M. Asta, L.-W. Wang, Machine learning force field for Fe-H system and investigation on role of hydrogen on the crack propagation in α-Fe, Comput. Mater. Sci. 214 (2022) 111709.
[44] L.B. Peral, I. Fernández-Pariente, C. Colombo, Critical hydrogen concentration for crack propagation in a CrMo steel: targeted experiments for accurate numerical modelling, Eng. Fract. Mech. 273 (2022) 108764.
[45] N.Z. Carr, R.B. McLellan, Hydrogen–vacancy interactions in Ni–H solid solutions, J. Phys. Chem. Solid. 67 (8) (2006) 1797–1802.
[46] K. Takai, H. Shoda, H. Suzuki, M. Nagumo, Lattice defects dominating hydrogen-related failure of metals, Acta Mater. 56 (18) (2008) 5158–5167.
[47] Y. Murakami, T. Kanezaki, Y. Mine, Hydrogen effect against hydrogen embrittlement, Metall. Mater. Trans. 41 (10) (2010) 2548–2562.
[48] P.J. Ferreira, I.M. Robertson, H.K. Birnbaum, Hydrogen effects on the interaction between dislocations, Acta Mater. 46 (5) (1998) 1749–1757.